Article

Customizable design strategies for high-performance bioanodes in bioelectrochemical systems

Customizable 3D-printing ink

GO sheet
Ferric ions
Magnetite nanoparticles

3D Printing

3D-printed bioelectrode

Anions
Cations
Geobacter sulfurreducens

Yu-Ting He, Qian Fu, Yuan Pang, ..., Wei Sun, Qiang Liao, Uwe Schröder

fuqian@cqu.edu.cn (Q.F.)
pangyuan31@mail.tsinghua.edu.cn (Y.P.)

HIGHLIGHTS

A 3D-printed graphene aerogel electrode was proposed for BESs

The optimized electrode mass transfer resistance was less than 5% of carbon felt

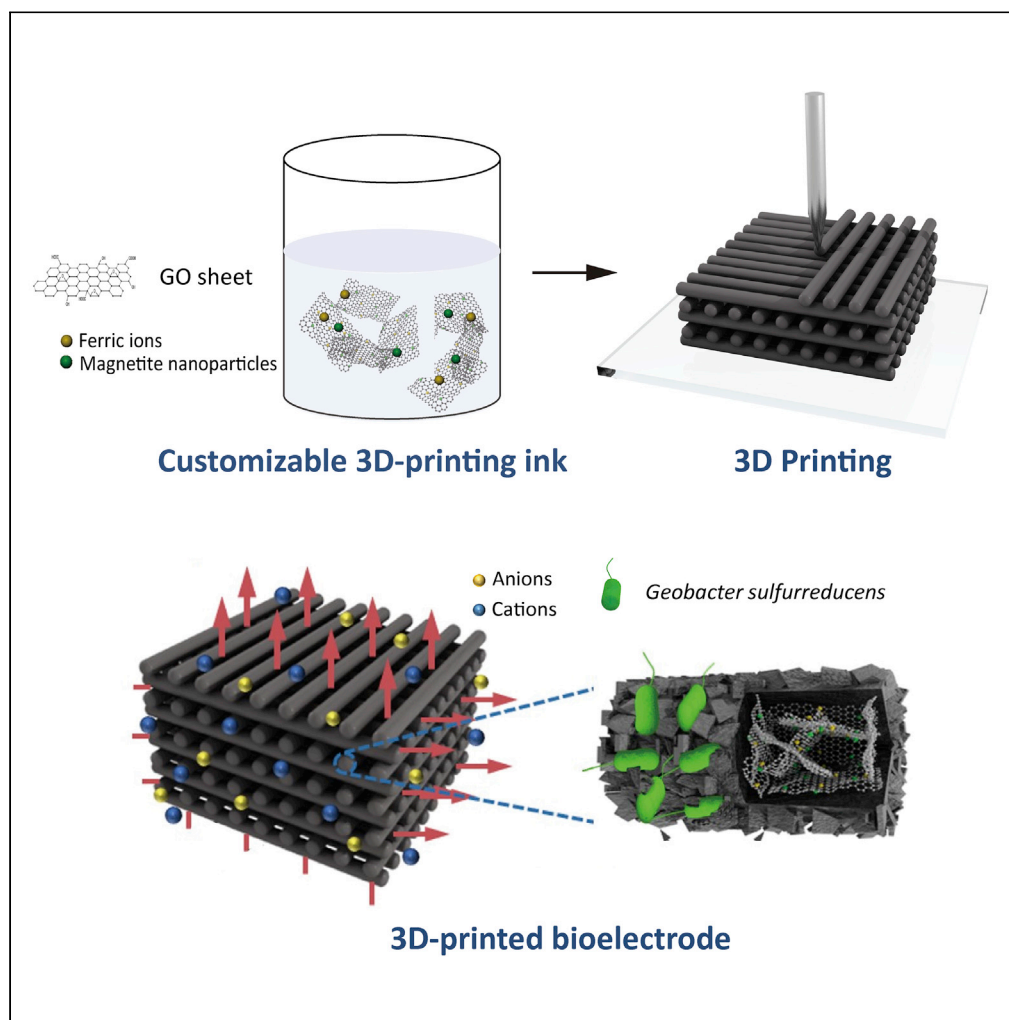A high volumetric current density of $10{,}608 \pm 1{,}036$ A/m^3 was achieved

Article

Customizable design strategies for high-performance bioanodes in bioelectrochemical systems

Yu-Ting He,[1,2] Qian Fu,[1,2,6,]* Yuan Pang,[3,4,]* Qing Li,[1,2] Jun Li,[1,2] Xun Zhu,[1,2] Ren-Hao Lu,[3,4] Wei Sun,[3,4] Qiang Liao,[1,2] and Uwe Schröder[5]

SUMMARY

Bioelectrochemical systems (BESs) can fulfill the demand for renewable energy and wastewater treatment but still face significant challenges to improve their overall performance. Core efforts have been made to enhance the bioelectrode performance, yet, previous approaches are fragmented and have limited applicability, unable to flexibly adjust physicochemical and structural properties of electrodes for specific requirements in various applications. Here, we propose a facile electrode design strategy that integrates three-dimensional printing technology and functionalized modular electrode materials. A customized graphene-based electrode with hierarchical pores and functionalized components (i.e., ferric ions and magnetite nanoparticles) was fabricated. Owing to efficient mass and electron transfer, a high volumetric current density of $10{,}608 \pm 1{,}036$ A/m^3 was achieved, the highest volumetric current density with pure *Geobacter sulfurreducens* to date. This strategy can be readily applied to existing BESs (e.g., microbial fuel cells and microbial electrosynthesis) and provide a feasibility for practical application.

INTRODUCTION

The accelerating modern consumption of traditional fossil energy and concomitant environmental deterioration have resulted in an urgent need for alternative energy sources and technologies (Rahimnejad et al., 2011). Bioelectrochemical systems (BESs) are emerging renewable technologies that can convert energy through the metabolism of electroactive bacteria (Gul and Ahmad, 2019; Logan et al., 2019), which have been exploited for diverse technologies, such as renewable energy generation (Sun et al., 2008), wastewater treatment (Du et al., 2007), biosensors (Kumlanghan et al., 2007), and bioremediation (Morris and Jin, 2007).

Despite several attempts enhance the performance of BESs, there remains a clear discrepancy between this prospective technology and real-world applications due to their relatively low power density output (Santoro et al., 2017). Apart from a vast array of factors (e.g., electroactive bacteria species, reactor architectures, ion exchange membranes, and substrates), bioelectrodes are considered the key factor in determining BES performance (Slate et al., 2019). Bioelectrodes serve as a platform where electroactive bacteria can exchange electrons, while providing a suitable environment for bacterial colonization and proliferation (Palanisamy et al., 2019). Therefore, the physicochemical properties and structure of electrodes significantly influence the electron transfer at the biological/inorganic interface and determine the maximum available surface area for electroactive bacteria attachment and growth. Previous studies have focused on high-performance electrodes with good biocompatibility and conductivity (Liu et al., 2020; Palanisamy et al., 2019; Rusli et al., 2019; Santoro et al., 2017; Slate et al., 2019), such as carbon cloth, graphite rod, carbon sponges, and metal oxide foams with conductive coatings (e.g., polypyrrole and poly (3, 4-ethylenedioxythiophene)) (Lv et al., 2013; Wang et al., 2013). Among them, porous electrodes are particularly promising, owing to their large surface area available for the adhesion and proliferation of bacteria. Nevertheless, pore clogging frequently occurs when using porous electrodes during the development of biofilms (Chong et al., 2019). Consequently, the transport of substrates and waste products inside 3D electrodes is largely restricted, resulting in ineffective pore utilization (i.e., an inert zone without bacteria) inside the electrodes, hindering performance improvement, contrary to the original intention of utilizing
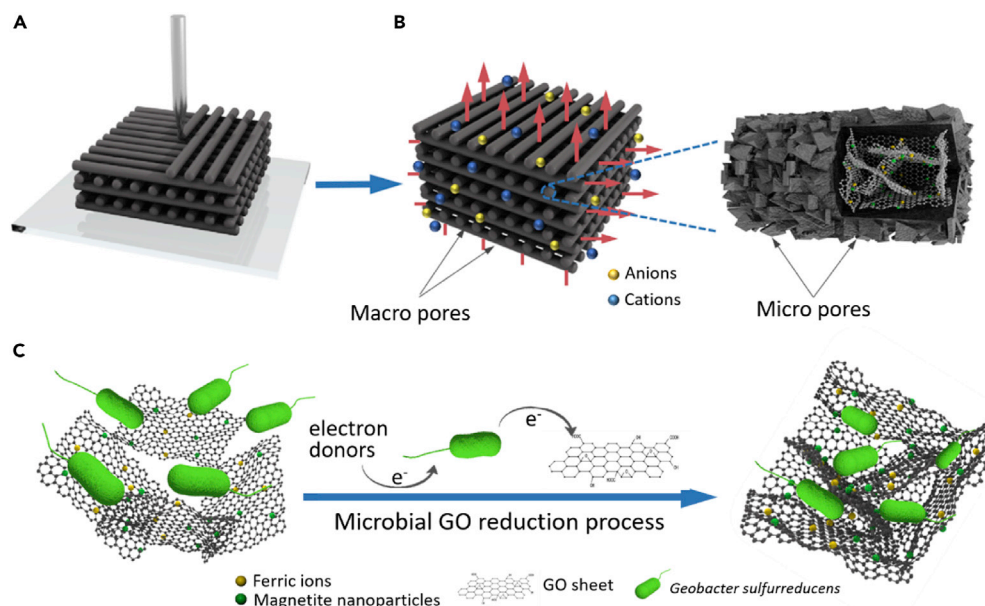
Figure 1. Schematic illustration of 3D printing process and microbial GO reduction
(A) The customized GO-based ink was printed into a designed structure.
(B) Schematic illustration of the 3D-printed electrode hierarchical pores.
(C) Schematic illustration of the microbial GO reduction process.

the large surface area of 3D porous electrodes. The random, long-distance, zigzag ion migration paths of the disordered electrode porous structure could hinder the rate of substrate transport and waste product removal, despite the biofilm not being completely clogged (Chen et al., 2012; Sun et al., 2017).

Three dimensional printing technology, which enables the fabrication of customizable 3D electrodes with expected geometric structures and channel sizes, can be used to explore a desired 3D electrode (Theodosiou et al., 2018, 2020). Recently, Bian et al. constructed a 3D-printed porous carbon anode using a carbonized UV-curable polymer resin with enhanced power generation in microbial fuel cells (MFCs) (Bian et al., 2018). Freyman et al. incorporated living electroactive bacteria (*Shewanella Oneidensis*) into 3D printing ink with alginate and carbon black to implement a 3D-printed bacterial structure as a living electrode for MFC (Freyman et al., 2020). These studies demonstrate the potential of fabricating electrodes via 3D printing technology; however, the low electron transfer rate at the biological/inorganic interface and the relatively low specific surface area available for bacterial adhesion limits power density. Therefore, the development of a high-performance bioelectrode with excellent biocompatibility, good conductivity, and optimized architecture for effective mass transfer is of great significance.

Herein, we demonstrate, to the best of our knowledge, for the first time a high-performance bioelectrode with designed 3D structures was fabricated by an adjustable printing ink using an extrusion-based 3D printing method. The customized ink for bioelectrode preparation consisted of well-dispersed graphene, ferric ions, and magnetite nanoparticles. Specifically, graphene oxide (GO) was selected as the primary component of the 3D printer ink, as its nanostructure can facilitate the electron transfer at the biological/inorganic interface (Li et al., 2012), and provide a large surface area for the adherence and proliferation of bacteria (Ren et al., 2016). Ferric ions and magnetite nanoparticles were incorporated as modular functional components into the 3D printer ink to promote bacterial growth and interfacial electron transfer (Cruz Viggi et al., 2014; Liu et al., 2018). Using extrusion-based 3D printing technology (Figure 1A) followed by freeze-drying for further pore formation, we obtained an integral composite GO aerogel electrode with hierarchical pores (macropores and micropores) (Figure 1B). The periodic macropores (>500 μm) of 3D printing frame structure, whose sizes were determined by the distance between the two nearby printed wires, were designed to provide open channels that can offer highly effective supply of nutrients and dissipation of waste inside and outside the electrode. The micropores (<100 μm) derived from graphene network on each printed wire significantly increased the bacterial colonization and proliferation surface area and can
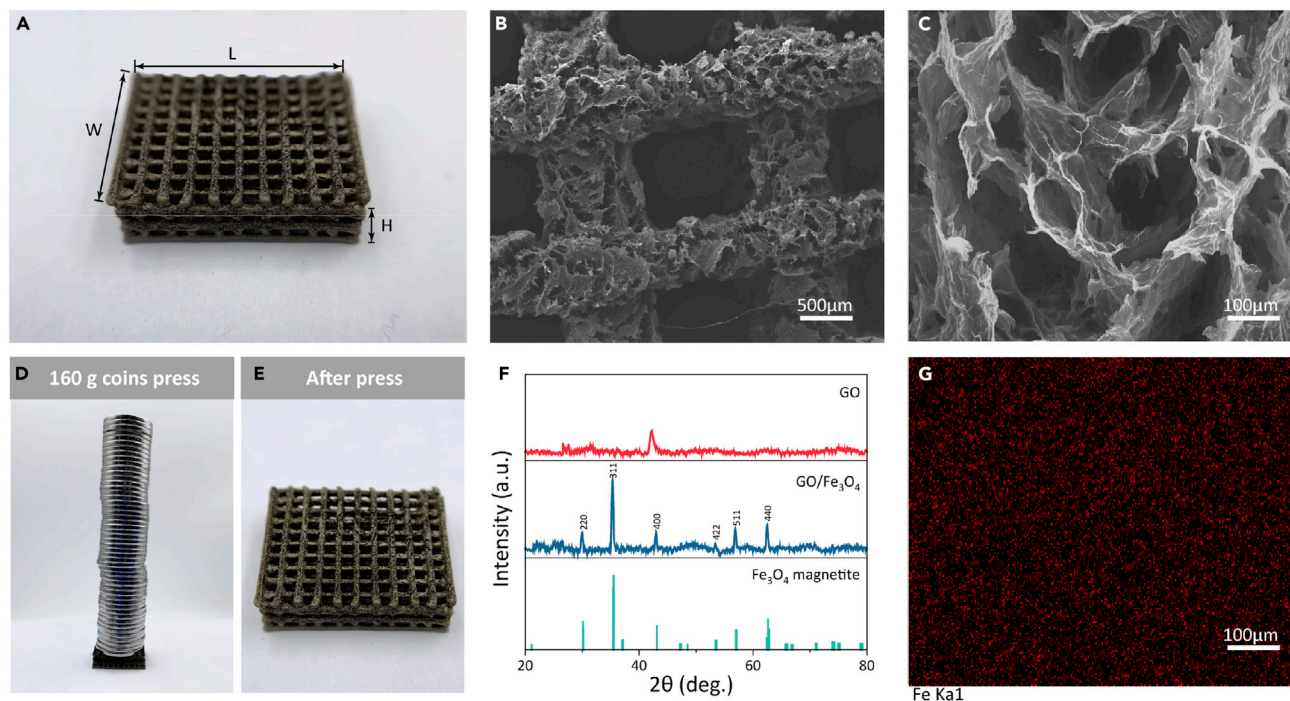
Figure 2. Morphology and characterization of 3D-Printed GO aerogel electrodes
(A) Photographical image of a typical GO aerogel electrode.
(B and C) SEM images of the hierarchical porous structure.
(D and E) Strength test of the GO aerogel electrodes pressed by 50 coins (∼160 g weight).
(F) XRD analyses of GO aerogel electrodes.
(G) Energy dispersive spectrum elemental map of iron for GO aerogel electrode corresponding to the SEM image.

promote permeation of the substrate. Moreover, the non-conductive GO electrode could be converted *in situ* into a conductive graphene anode via an electroactive bacterial respiration process (Figure 1C) (De Silva et al., 2017). In this process, only Geobacter *sulfurreducens* were used for GO reduction, eliminating extra chemical conversion processes. Our work provides a facile strategy for an easily controllable, flexible, and highly producible bioelectrode fabrication, opening a new path to enhance the performance of BESs and related microbial electrochemical technologies.

RESULTS

Morphology and characterization of 3D-printed GO aerogel electrodes

The electrode ink must possess a shear-thinning behavior to enable continuous extrusion and a suitable modulus to hold the expected structure. The ferric ions added to the customized ink can act as cross-linkers, as they can form electrostatic interactions and coordination bonds with negatively charged GO sheets (i.e., their carboxylic and hydroxyl functional groups (Jiang et al., 2018; Zhao et al., 2017). The resultant GO hydrogel inks showed a higher apparent viscosity with a clear shear-thinning behavior and higher storage modulus magnitudes, in comparison with pure GO solutions (Figure S1, Supplemental Information (SI)). Following the layer-by-layer 3D printing process and freeze-drying process, 3D-printed GO aerogel electrodes (1.6 cm in width, 2 cm in length, and 4 mm in thickness) with a lattice structure were obtained, as shown in Figure 2A. The open channel structure was easily observed from the top and the side (Figure S2, Supplemental Information). Figures 2B and 2C show representative scanning electron microscope (SEM) images of the 3D-printed GO aerogel electrode. It is obvious that the GO aerogel electrode possesses hierarchical pores, including macropores (∼hundreds of micrometers, up to the mm scale) between the two neighboring printed wires and micropores (∼tens of micrometers) on each wire of the aerogel. The macropores are designed to enable efficient mass transfer of substrates, while micropores enhancing the specific surface area, and promote the attachment and growth of electroactive bacteria. The strength test (Figures 2D and 2E) shows that the GO aerogel electrode can support 50 coins (∼160 g weight) without a clear shape
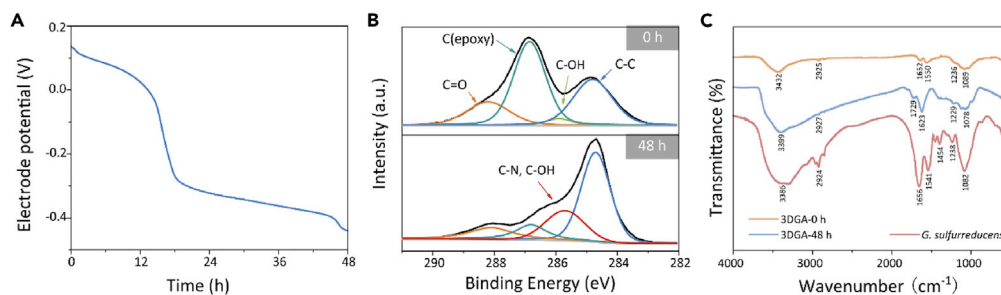
Figure 3. Characterization of microbial reduced graphene

(A) Variation of the potential (*vs.* Ag/AgCl) of a 3D-printed rGO aerogel electrode with time at an open circuit condition after the inoculation with *G. sulfurreducens*.

(B) XPS spectra of the 3D-printed rGO electrode before (0 hr) and after (48 hr) the microbial reduction by *G. sulfurreducens*.

(C) FTIR spectra of *G. sulfurreducens*, and the 3D-printed rGO electrode before (0 hr) and after (48 hr) the microbial reduction.

change and damage. The X-ray diffraction (XRD) electrode pattern (Figure S3, Supplemental Information) shows the characteristic peaks at around 10.9° that were indexed to GO. In addition, the characteristic diffraction peaks at diffraction angles of 30.06°, 35.32°, 42.98°, 53.37°, 56.87°, and 62.51° (Figure 2F) correspond to the (220), (311), (400), (422), (511), and (440) crystal surfaces, respectively, which can be indexed to Fe_3O_4 nanoparticles (JCPDS 75–1609) (Zhao et al., 2010). X-ray photoelectron spectroscopy (XPS) analysis revealed the presence of Fe, C, and O elements inside the GO aerogel electrode (Figure S4A, Supplemental Information). In the high-resolution XPS spectra of Fe 2p (Figure S4B, Supplemental Information), the GO aerogel electrode clearly exhibited five peaks: $2p_{3/2}$ of Fe (III) ions, $2p_{1/2}$ of Fe (III) ions, $2p_{3/2}$ of Fe (II) ions, $2p_{1/2}$ of Fe (II) ions, and their satellite peaks, indicating the coexistence of Fe (II) and Fe (III) and hence the presence of Fe_3O_4. Energy-dispersive spectrum mapping (Figure 2G) showed a uniform distribution of iron corresponding to the SEM image (Fig C).

In situ microbial reduction of 3D-printed GO aerogel electrodes

The low conductivity of GO, caused by the destruction of its π-conjugated structure, does not meet the requirements of an electrode for efficient electron transfer and electron conduction. Therefore, the 3D-printed GO electrodes must be reduced to rGO electrodes with high conductivity. Recent studies have shown that several electroactive bacteria (e.g., *Shewanella* (Salas et al., 2010)) are capable of directly utilizing GO as the extracellular electron acceptor for the reduction of GO to rGO. The microbially reduced graphene possessed better biological properties (e.g., biocompatibility) than chemically reduced graphene, exhibiting significantly enhanced microbial electricity generation owing to the formation of bacteria/graphene scaffolds (Fan et al., 2014; Virdis and Dennis, 2017). Herein, the GO electrode was microbially reduced to graphene by keeping bioelectrochemical reactors under open circuit conditions following *G. sulfurreducens* inoculation. As shown in Figure 3A, the potential of the GO electrode decreased with operating time, suggesting the colonization and growth of *G. sulfurreducens* on the surface of the GO electrode (Geelhoed and Stams, 2011), and the concomitant reduction of GO to rGO by *G. sulfurreducens*. After 48 hr of inoculation, rGO formation and its interaction with bacteria were investigated by chemical tests.

Figure 3B shows the high-resolution C1s XPS spectrum of the rGO electrodes. Before the inoculation of *G. sulfurreducens*, four peaks at 284.8, 285.9, 286.9, and 288.2 eV were clearly resolved by fitting experimental data. The peak at 284.8 eV is a typical C-C bond value in C1s, which exists in graphene and graphite. The peaks at 285.9, 286.9, and 288.2 eV are consistent with the C1s binding energy in C-OH, epoxy (C-O), and C=O, respectively (Lei et al., 2012; Mai et al., 2011). In contrast, the intensity of the C-C peak increased following cultivation for 48 hr, indicating that the sp^2 carbon character of graphite was restored, and the GO was successfully reduced during the microbial reduction process. The intensity of the peaks corresponding to oxygen-containing functional groups of the electrodes became much weaker, while the peak at 285.8 eV (corresponding to C-N, C-OH) increased following the microbial reduction process. This can possibly be ascribed to the formation of C-N, whose binding energy was close to that of C-OH. As shown in the high-resolution N1s (Figure S5B, Supplemental Information), a peak at 399.9 eV (assigned to C–N) was observed (Zhao et al., 2019), further revealing the formation of C–N bonds during the microbial reduction

of GO. The results of the Raman test (Figure S6, Supplemental Information) also confirmed the successful reduction of GO, as the intensity ratio value (1.08) of the disorder D peak to the graphitic G peak (I_D/I_G) increased in contrast to that of GO (0.88), which can be ascribed to the presence of unrepaired defects following the removal of partial oxygen groups. In addition, the XPS spectrum of the rGO electrode interior also showed an increased C-C peak intensity at 284.8 eV post-cultivation for 48 hr (Figure S7, Supplemental Information), indicating an efficient GO reduction of the entire electrode.

To further investigate the reduction of GO electrodes and the colonization of *G. sulfurreducens*, we performed an Fourier transform infrared (FTIR) analysis of GO, rGO, and *G. sulfurreducens*. The spectrum (Figure 3C) of the original GO sample showed a number of peaks corresponding to oxygenated functional groups, including the alkoxy C-O (1,078 cm^{-1}), epoxy C-O (1,229 cm^{-1}), C=O (1,729 cm^{-1}), and O-H peak (3,399 cm^{-1}). In contrast, C-O, C=O, and O-H oxygenated functional groups significantly decreased after the microbial reduction process. The *G. sulfurreducens* sample exhibited special peaks, such as the 1,541 cm^{-1} region (closely corresponding to the N-H and C-N from amide) and the region at around 1,656 cm^{-1} (associated with the C=O from amide). Notably, the FTIR spectrum of the rGO electrode showed a comprehensive characteristic line, resulting from GO and *G. sulfurreducens* samples, reflecting the colonization of *G. sulfurreducens* on the surfaces of the rGO electrode. The potential source for these amide groups in the rGO sample was probably *G. sulfurreducens,* as well as their extracellular polymeric substances on the surface of the electrodes, which were in accordance with those of previous studies (Chen and Chen, 2015; Lee and Hur, 2016). Moreover, the electroactive accessible surface area (ECSA) of rGO aerogel and carbon felt anode were estimated by the cyclic voltammetry (CV) with $K_3[Fe(CN)_6]$ solution (Figure S8, Supplemental Information). The rGO aerogel anode exhibited the highest peak current density of 90.79 A/m^2, with a corresponding ECSA of 18.31 cm^2/cm^2 (subject to the surface area of the electrodes), which was about four times larger than that of carbon felt and much higher than that of the modified carbon cloth in previous studies (Table S1, Supplemental Information). The results indicated that the 3D-printed rGO aerogel electrode can provide more electrochemically active sites to accept electrons from *G. sulfurreducens*.

BES performance with customized composite electrodes

To evaluate the bioelectrochemical performance of the customized composite electrodes, four kinds of rGO aerogel electrodes were fabricated by altering the composition of the printing ink with/without the addition of ferric ion or magnetite nanoparticles, represented by rGO, rGO/Fe^{3+}, rGO/Fe_3O_4, and rGO/Fe^{3+}/Fe_3O_4 aerogel electrodes, respectively. Following the open circuit-based microbial reduction of GO, all the electrodes were poised at 50 mV *vs.* Ag/AgCl for current generation.

Figure 4A illustrates the current generation of bioelectrochemical reactors using rGO, rGO/Fe^{3+}, rGO/Fe_3O_4, and rGO/Fe^{3+}/Fe_3O_4 aerogel, as well as carbon felt as anodes. A repeatable current generation was obtained 13 days post cultivation, indicating successful bioanode start-up. The maximum current density of each rGO aerogel bioanode was at least two times higher than that of the conventional 3D carbon felt anode, suggesting the excellent properties of rGO as an electrode material. Notably, the rGO/Fe^{3+}/Fe_3O_4 aerogel bioanode achieved the highest maximum current generation of 18.99 $\pm$ 2.28 A/m^2, which was 44.3, 29.4, 13.4% higher than that of the rGO, rGO/Fe^{3+}, rGO/Fe_3O_4 aerogel anodes, respectively. These results indicate that the combination of graphene, ferric ions, and magnetite nanoparticles all had positive effects on the formation of biofilm or the proliferation of *G. sulfurreducens*, and there perhaps existed a synergistic effect between ferric ions and magnetite nanoparticles on promoting biocatalysis.

Cyclic voltammetry (Figure 4B) of bioanodes under turnover conditions illustrated a similar sigmoidal shape for all the rGO aerogel anodes in the scan range of −0.6 to 0.4 V, demonstrating the catalytic oxidation of acetate by the biofilms on these bioelectrodes in contrast to the abiotic control electrode (Figure S9A, Supplemental Information). Interestingly, the first derivative of the cyclic voltammograms clearly showed that the redox active potential range changed. The rGO, rGO/Fe^{3+}, rGO/Fe_3O_4, and rGO/Fe^{3+}/Fe_3O_4 biofilm aerogel anodes exhibited increasing electroactivity over a wider potential range from −0.47 to −0.25 V, while the redox active potential range for carbon felt was narrower from −0.4 to −0.25 V, indicating that the *G. sulfurreducens* electron transfer could probably be changed using 3D-printed rGO aerogel anodes.

To further investigate the electron transfer, differential pulse voltammetry (DPV)diff was performed in depleted sodium acetate culture medium. Figure 4C shows the different oxidation peaks for the different
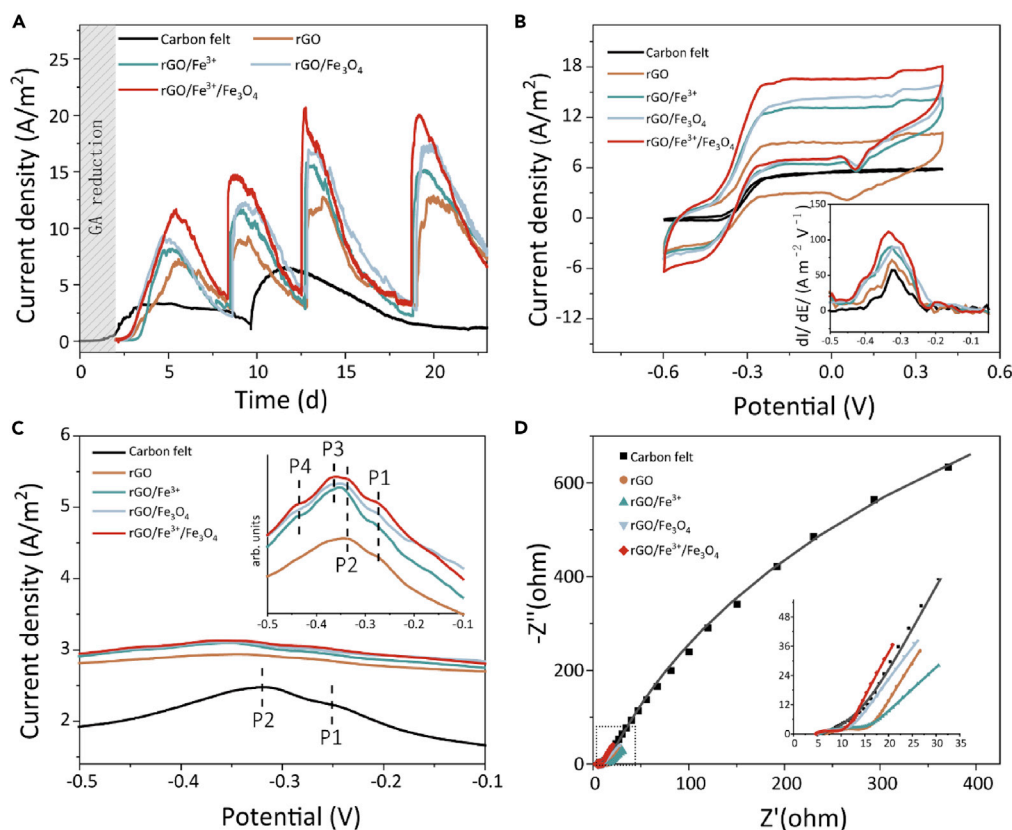
Figure 4. Electrochemical characteristics of carbon felt, rGO, rGO/Fe^{3+}, rGO/Fe$_3$O$_4$, and rGO/Fe^{3+}/Fe$_3$O$_4$ aerogel bioanodes

(A) Current generation under a constant potential of 50 mV *vs.* Ag/AgCl.

(B) Cyclic voltammetry (CV) under turnover conditions in a PBS solution (50 mM, pH = 7.2) containing 3.38 g/L acetate at 0.1 mV/s (the inset plots show the first derivative of cyclic voltammograms).

(C) Differential pulse voltammetry (DPV) characterized in acetate-free PBS solution with 300 ms pulse width, 50 mV amplitude, 2,000 ms step time, and 0.5 mV step height.

(D) Electrochemical impedance spectroscopy (EIS) analysis characterized at a working potential of 50 mV vs. Ag/AgCl from 100 kHz to 10 mHz at AC amplitude of 10 mV.

samples of the bioanodes. Two dominant oxidation peaks at −0.25 and −0.31 V were observed in the carbon-felt bioanode, while two new oxidation peaks (i.e., p3 at −0.43 V and p4 at −0.38 V) appeared in the DPV of the 3D printed rGO aerogel bioanodes. In contrast, no clear redox peak was observed in the DPV of the bare rGO/Fe$_3$O$_4$ aerogel electrode prior to *G. sulfurreducens* inoculation, suggesting the contribution of *G. sulfurreducens* to the oxidation peaks (Figure S9B, Supplemental Information). Interestingly, the potential of the p3 and p4 peaks were close to the midpoint potentials of typical cytochrome OmcZ −0.42 V), OmcB (−0.39 V), OmcS (−0.43 V), and periplasmic cytochrome PpcA (−0.37 V) of *G. sulfurreducens* (Katuri et al., 2010; Zhu et al., 2012). The results indicated that the ferric ions probably have positive effects on the synthesis of *c*-type cytochromes, which could promote electron transfer and thus enhance the performance of bioanodes (Zhao et al., 2016).

Figure 4D shows the Electrochemical impedance spectroscopy (EIS) analysis of the bioanodes. The semicircle portion at high frequency corresponded to the interfacial charge transfer resistance (R$_{ct}$). For the rGO aerogel anodes (10.75 Ω for rGO, 10.67 Ω for rGO/Fe^{3+}, 8.45 Ω for rGO/Fe$_3$O$_4$, 8.26 Ω for rGO/Fe^{3+}/Fe$_3$O$_4$), the R$_{ct}$ values were smaller than the carbon felt bioanode (15.45 Ω), and the rGO/Fe^{3+}/Fe$_3$O$_4$ aerogel anode showed the smallest R$_{ct}$, which was beneficial for the electron transfer from bacteria to the solid anode (Table S2, Supplemental Information). The curve at low frequency represents the mass transfer resistance (R$_{mt}$), and the R$_{mt}$ of the rGO aerogel anodes (987 Ω for rGO, 896 Ω for rGO/Fe^{3+}, 945 Ω for rGO/Fe$_3$O$_4$, 953 Ω for rGO/Fe^{3+}/Fe$_3$O$_4$) was much lower than that of the carbon felt group (2382 Ω), indicating
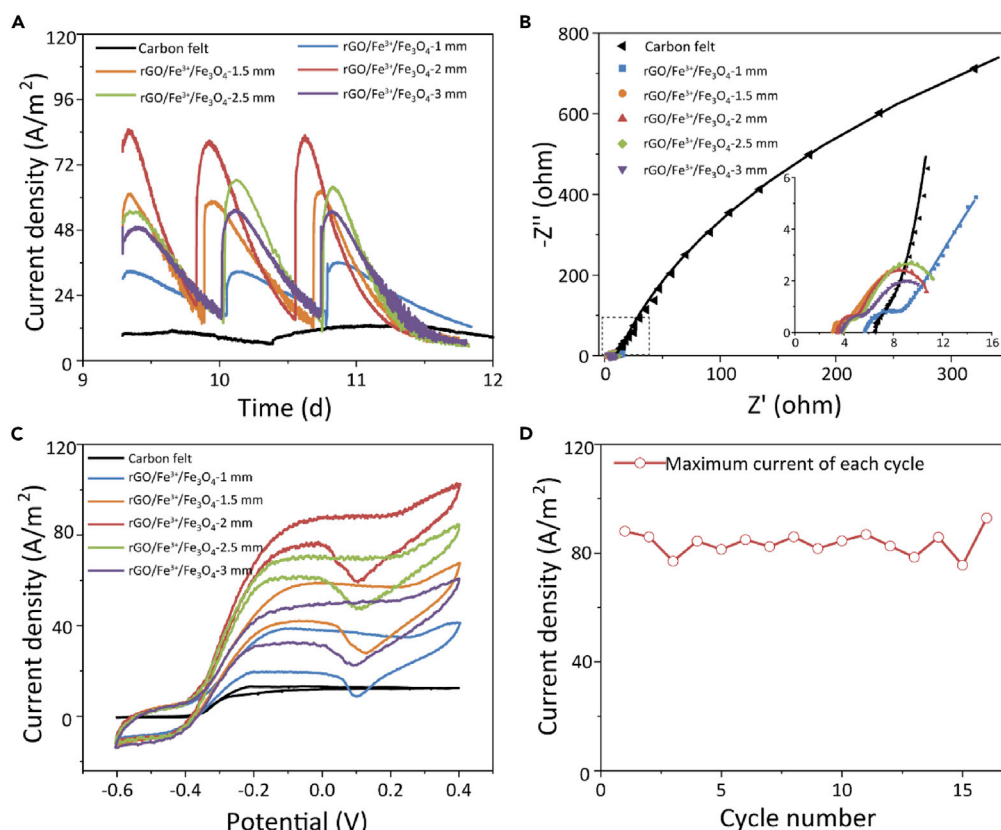
Figure 5. Electrochemical characteristics of 3D-printed rGO/Fe^{3+}/Fe$_3$O$_4$ anodes with different channel sizes and carbon felt anode

(A) Current generation under a constant potential of 50 mV vs. Ag/AgCl.

(B) EIS characterized at a working potential of 50 mV, recording from 100 kHz to 10 mHz at AC amplitude of 10 mV.

(C) CV in a PBS solution (50 mM, pH = 7.2) containing 3.38 g/L acetate at 0.1 mV/s.

(D) Long-term current generation of rGO/Fe^{3+}/Fe$_3$O$_4$-2mm anode in a batch mode (400 hr).

that the interconnected porous structure of the rGO aerogel electrode was beneficial for mass transfer to some degree. This customized composite rGO/Fe^{3+}/Fe$_3$O$_4$ electrode acts as an excellent carrier of bio-catalysts for high performance.

Optimization of the channel size of 3D-printed rGO aerogel electrodes

As mentioned above, microscale pores are prone to be clogged by the growing biofilm, which is the primary reason for the insufficient utilization of the inner zone in typical 3D electrodes. Therefore, to exploit the internal surface of rGO/Fe^{3+}/Fe$_3$O$_4$ aerogel electrode and to enable efficient mass transfer into the 3D structure, we designed five kinds of rGO/Fe^{3+}/Fe$_3$O$_4$ aerogel electrodes with different channel sizes, according to the distance between the two nearby 3D-printed wires (i.e., 1, 1.5, 2, 2.5, and 3 mm). All these 3D rGO/Fe^{3+}/Fe$_3$O$_4$ electrodes possessed hierarchical porous structures ranging from nanometers to millimeters, and the thickness of all the electrodes was 8 mm. Figure 5A shows the current generation of rGO/Fe^{3+}/Fe$_3$O$_4$ aerogel anodes with different channel sizes after nine days of operation. With the increase in the channel size of the rGO aerogel electrodes, the maximum current generation exhibited a tendency of increasing first and then decreasing. The maximum projected current density (84.9 ± 8.3 A/m^2) (equals to 10,608 ± 1,036 A/m^3 of volumetric current density) was achieved by rGO/Fe^{3+}/Fe$_3$O$_4$-2mm electrode, which is 7.9-fold higher than that (10.8 ± 2.2 A/m^2) of carbon felt with the same thickness. To our knowledge, the volumetric current density (10,608 ± 1,036 A/m^3) in this study had the highest values for pure culture of *G. sulfurreducens* to date and was much higher than that of most previously reported bioanodes (Table 1). Then, the bioelectrocatalytic activity of the anodes was further identified using CV. From

Table 1. Comparisons of the performance of 3D porous anodes

Anode	Operating conditions	Inoculation/substrate	Anode performance		Reference
			Projected current density(A/m^2)	Volumetric current density (A/m^3)	
Graphene/polyacrylamide	Single chamber, batch fed, 30°C	Mixed culture,1 g/L acetate	3.6	251.7	(Chen et al., 2019)
FeS$_2$-decorated graphene	H-cell, batch fed, 37°C	Mixed culture, 2 g/L acetate	3.06	/	(Wang et al., 2018)
Onion	Single chamber, discontinuous mode, 30°C	Mixed culture, 1 g/L acetate	9.77	/	(Li et al., 2018)
3D porous CNT sponge	H-cell, batch fed, room temperature	Mixed culture, 1 g/L acetate	6.51	2170	(Xu et al., 2019)
CNT/PANI modified graphite felt	H-cell, batch fed, 30°C	Mixed culture, 1.64 g/L acetate	1.9	95	(Cui et al., 2015)
3D-weaved carbon mesh anode	H-cell, continuous mode (2.17 mL/min)	*G. sulfurreducens*, 0.64 g/L acetate	/	22.6	(Luo et al., 2020)
Polydopamine-decorated graphitic carbon foam	H-cell, batch fed	*S. putrefaciens* cells, 1.6 g/L lactate	10.6	3533	(Jiang et al., 2017)
3D printed carbonaceous porous anode	Single chamber, batch fed, room temperature	*S. Oneidensis MR-1*, 1.6 g/L lactate	1.72	344	(Bian et al., 2018)
3D-printed carbon black-decorated alginate living electrode	H-cell, batch fed	*S. Oneidensis MR-1*, Tryptic soy broth	0.092	18.5	(Freyman et al., 2020)
3D-printed Fe$_3$O$_4$-decorated graphene	H-cell, batch fed, 30°C	*G. sulfurreducens*, 2 g/L acetate	84.9	10,608 ± 1,036	current study

CNT, carbon nanotubes; PANI, polyaniline.

Figure 5B, it is apparent that the biocatalytic current densities were in the same order as well as stable current densities. Notably, when the pore size was reduced by 0.5 mm from 2 mm to 1.5 mm, the biocatalytic current density of rGO/Fe^{3+}/Fe$_3$O$_4$ decreased by 33%, which was thought to be a limitation of substance transfer in the pore size of 1.5 mm.

EIS tests were performed to investigate the performance of these graphene electrodes with different channel sizes. As shown in Figures 5C and Table S3 (Supplemental Information), the mass transfer resistance of carbon felt was 2,854.2 Ω, which accounted for almost 99% of the total resistance (2,872.1 Ω). In contrast, the mass transfer resistance of rGO aerogel anodes was less than 5% of that of carbon felt, suggesting that the lattice structure of the rGO aerogel fabricated by 3D printing significantly reduced the mass transfer resistance. The mass transfer resistance of the rGO aerogel anodes varied with the channel size. The mass transfer resistance of rGO aerogel anodes decreased by an order of magnitude from 115.6 Ω for rGO/Fe^{3+}/Fe$_3$O$_4$-1mm to 11.0 Ω for rGO/Fe^{3+}/Fe$_3$O$_4$-1.5mm. When the channel size of the rGO aerogel electrode continued to increase, the mass transfer resistance decreased to 6.9, 6.5, and 6.4 Ω, corresponding to rGO/Fe^{3+}/Fe$_3$O$_4$-2mm, rGO/Fe^{3+}/Fe$_3$O$_4$-2.5mm, and rGO/Fe^{3+}/Fe$_3$O$_4$-3mm (Table S3, Supplemental Information), respectively. The results of EIS analysis strongly suggested that the electrode structure was the primary determinant of mass transfer. The value of mass transfer resistance was significantly reduced when the pore size was raised close to the millimeter scale and almost stabilized when the pore sizes continued to increase, indicating that the pore size at the millimeter scale could assure an adequate mass transfer for bioanodes, resulting in the highest current density of rGO/Fe^{3+}/Fe$_3$O$_4$-2mm.

To further elaborate the influence of pore size, the structure and morphology of the biofilms on graphene anodes were subsequently characterized by SEM after 35 days of steady current generation. As shown in Figure 6, the entire surface of each 3D-printed graphene wire of all graphene anodes was covered with a thick and dense biofilm, in contrast to the relatively sparse biofilm on the carbon felt anode (Figure S11, Supplemental Information), and the 3D-printed macropores were not clogged by the biofilm after 1 month
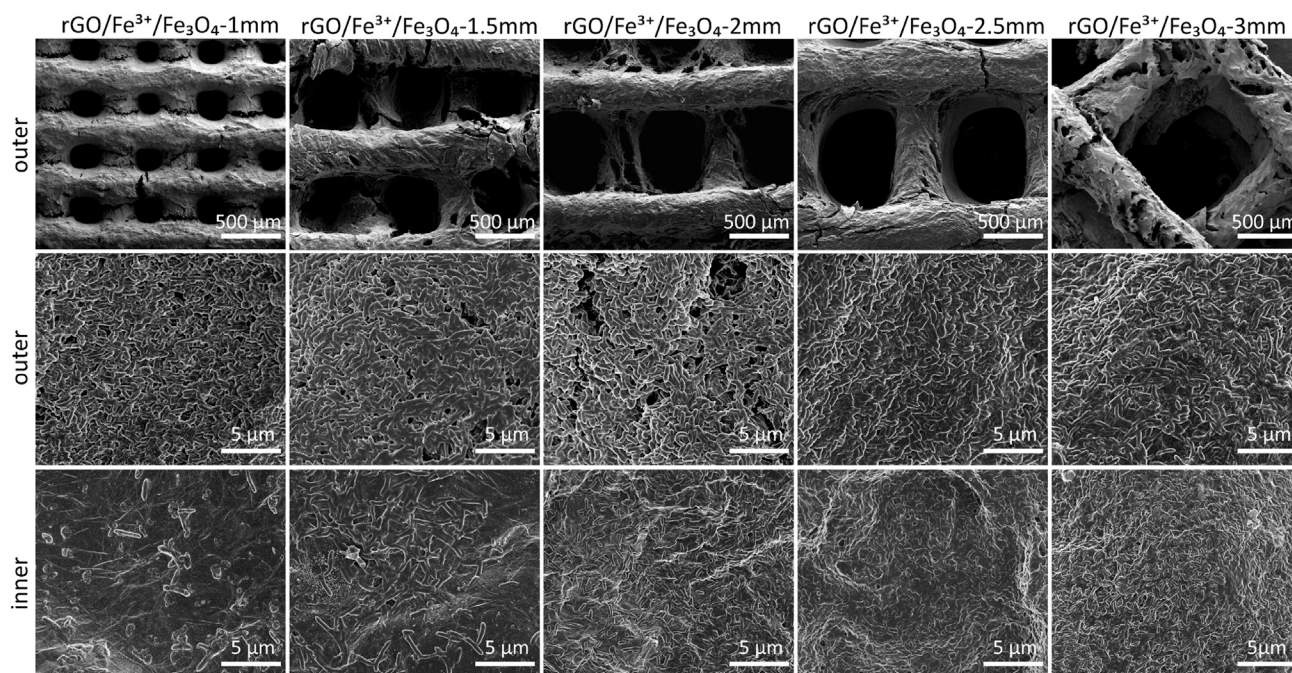
Figure 6. SEM images of biofilm formation for rGO/Fe^{3+}/Fe$_3$O$_4$ anodes with different channel sizes

of operation. The SEM images of the biofilm in the center of the graphene anodes show quite different morphologies. The internal biofilms of rGO/Fe^{3+}/Fe$_3$O$_4$-1mm to rGO/Fe^{3+}/Fe$_3$O$_4$-2mm appeared to increase density, and the internal biofilms appeared similar anew from the rGO/Fe^{3+}/Fe$_3$O$_4$-2mm to rGO/Fe^{3+}/Fe$_3$O$_4$-3mm, which was in accordance with the value of EIS analysis. The results indicated that the ordered macropores at the millimeter scale provided an unobstructed channel for a large population of bacteria to colonize while ensuring sufficient inter mass transfer of substrates and products. Generally, the channel size of the electrodes primarily affects the performance of bioelectrodes by influencing the biofilm formation and mass transfer in the electrodes, which also mutually influence each other. For a typical porous electrode, pores with a few tens of micrometers often become clogged during the growth and maturation of the biofilm, which can achieve a thickness of tens or hundreds of micrometers. According to a previous study on pores ranging from 100 to 500 μm (Chen et al., 2014; Yuan et al., 2013), the clogging can be avoided following long-term operation, while the mass transfer (primarily acetate and H$^+$), as the considerable rate-limiting step, will hinder the catalytic activity of bacteria in the internal of the electrode and restrict the overall performance, resulting in scattered bacteria or sparse biofilm inside of porous electrodes. Significantly, a thick and dense biofilm formed on the outside and inside of the rGO/Fe^{3+}/Fe$_3$O$_4$-2mm (Figures 6 and 7), indicating that this 3D-printed electrode provided a genuine 3D structure for biofilm development and effective mass transfer, thus guaranteeing the overall catalytic ability of *G. sulfurreducens* and achieving a remarkable current density.

To evaluate the long-term stability of the 3D-printed rGO bioanodes, a dual-chamber bioelectrochemical reactor using an rGO/Fe^{3+}/Fe$_3$O$_4$-2mm anode was operated for 400 hr with periodic medium exchange. Figure 5D illustrates the electricity generation cycle using rGO/Fe^{3+}/Fe$_3$O$_4$-2mm as the anode. The maximum current densities were relatively stable during 16 batch-feeding cycles, which could be attributed to the consistently sufficient mass transfer owing to the open channels. Moreover, the designed 3D-printed electrode was not destroyed and clogged during the operation. This demonstrates that the rGO/Fe^{3+}/Fe$_3$O$_4$-2mm anode can support a suitable environment for bacterial growth and achieve electricity generation in a long-term operation.

DISCUSSION

In this paper, we proposed and demonstrated a scalable strategy to fabricate a designed 3D structure electrode by functional tailored printing ink and the bioelectrode achieved an unprecedented high volumetric
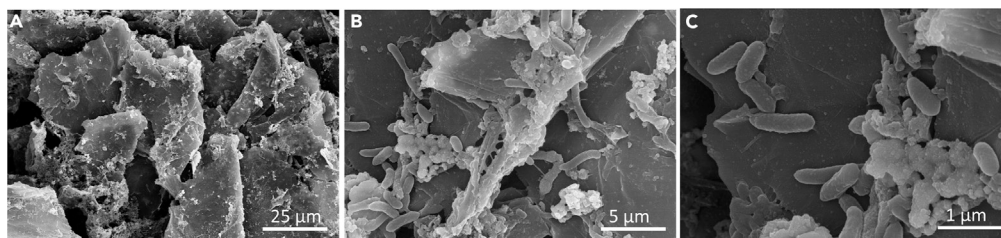
Figure 7. Cross section SEM images of one graphene wire located in the center of rGO/Fe^{3+}/Fe$_3$O$_4$-2mm electrode, indicating the presence of large quantities of attached bacteria on the graphene sheets

current density of 10,608 $\pm$ 1,036 A/m^3, the highest volumetric current density with pure *G. sulfurreducens* to date. This strategy brings new insights into electrode fabrication and has the merit of wide applicability in BESs. We can flexibly adjust the physicochemical and structural properties of electrode by simply altering the base component and functional modular components, such as polymeric matrices, redox species, or conductive nanomaterials. Besides, taking the advantage of 3D printing technology, we can freely fabricate electrodes with arbitrary structure for various demands in BESs, and it is expected to be a feasibility for scale-up application due to the high productivity of 3D printing technology.

Future development of electrode is necessary for scale-up and practical application of bioelectrochemical technique. During the past decades, there are considerable researches regarding the cellular microbiology (bioelectroecology of biofilm, electrons exchange and etc.), electrode (materials, structure, and etc.), reactor configuration, and operation parameters. Our strategy opens up opportunities to integrate the tremendous efforts so far, and achieve functional integration of BESs electrodes, which allows us to modularize major or critical function components of the electrode and match the electrode with the most appropriate properties for specific electrochemical application scenarios. Still, technologies based on electroactive microorganisms are in nascent stage, there is much left to be further explored.

Limitations of the study

The base component and functional modular components of the customized printing ink can be broadened to various materials (e.g., conductive polymer, nanoscale carbon) to endow the electrode with different characteristics. The interactions between different functional materials and electroactive microorganisms deserve to be further studied. This article shows the channel sizes close to millimeter scale can assure an adequate mass transfer and avoid clogging of *G. sulfurreducens* biofilm. For the optimization of channel sizes in other situations, the influence of electroactive microorganism species and system operation parameters needs to be further considered. In addition to experimental measurements, modeling and simulation work can be further integrated to provide theoretical guidance for the design of electrode structure.

CONCLUSION

In summary, we have demonstrated a strategy to fabricate a designed 3D structure electrode using a functionally tailored printer ink. The 3D printed rGO/Fe^{3+}/Fe$_3$O$_4$-2mm aerogel bioelectrode achieved an unprecedented high volumetric current density of 10,608 $\pm$ 1,036 A/m^3, which was 7.9-fold higher than that of the control carbon felt bioanode and was the highest volumetric current density with pure *G. sulfurreducens*. The mass transfer resistance of the optimized electrode was almost three orders of magnitude lower than that of the carbon felt. The SEM images and electrochemical analysis suggested that the high performance of rGO bioelectrodes was attributed to the hierarchical pores of the rGO aerogel, which ensured sufficient mass transfer of the substrate and high specific surface area for the attachment and growth of bacteria, and the addition of magnetite nanoparticles, which probably enhanced the interfacial electron transfer. This strategy provides new approaches for electrode fabrication and has a great potential for wide applicability in BESs.

Resources availability

Lead contact

Further information and requests for resources and reagents should be directed to and will be fulfilled by the lead contact, Qian Fu (fuqian@cqu.edu.cn)

Materials availability

This study did not generate new unique reagents.

Data and code availability

This study did not generate/analyze data sets/code.

METHODS

All methods can be found in the accompanying Transparent Methods supplemental file.

SUPPLEMENTAL INFORMATION

Supplemental information can be found online at https://doi.org/10.1016/j.isci.2021.102163.

AUTHOR CONTRIBUTIONS

Y.T.H., Q.F., and Y.P. conceived the idea. Y.T.H. and Q.F. designed the experiments. Y.T.H. performed the main experiments. Q.L. and R.H.L. assisted in performing the experiments. Y.T.H., Q.F., and J.L. wrote the paper. U.S and Y.P. review and editing the paper. X.Z., W.S., and Q.L. supervised, administrated, and acquired the funding for the entire research.

DECLARATION OF INTERESTS

The authors declare no competing interests.

REFERENCES

Bian, B., Shi, D., Cai, X., Hu, M., Guo, Q., Zhang, C., Wang, Q., Sun, A.X., and Yang, J. (2018). 3D printed porous carbon anode for enhanced power generation in microbial fuel cell. Nano Energy *44*, 174–180.

Chen, W., Huang, Y.-X., Li, D.-B., Yu, H.-Q., and Yan, L. (2014). Preparation of a macroporous flexible three dimensional graphene sponge using an ice-template as the anode material for microbial fuel cells. RSC Adv. *4*, 21619–21624.

Chen, J.Y., Xie, P., and Zhang, Z.P. (2019). Reduced graphene oxide/polyacrylamide composite hydrogel scaffold as biocompatible anode for microbial fuel cell. Chem. Eng. J. *361*, 615–624.

Chen, S., He, G., Liu, Q., Harnisch, F., Zhou, Y., Chen, Y., Hanif, M., Wang, S., Peng, X., and Hou, H. (2012). Layered corrugated electrode macrostructures boost microbial bioelectrocatalysis. Energ. Environ. Sci. *5*, 9769–9772.

Chen, X., and Chen, B. (2015). Macroscopic and spectroscopic investigations of the adsorption of nitroaromatic compounds on graphene oxide,

reduced graphene oxide, and graphene nanosheets. Environ. Sci. Technol. *49*, 6181–6189.

Chong, P., Erable, B., and Bergel, A. (2019). Microbial anodes: what actually occurs inside pores? Int. J. Hydrogen Energ. *44*, 4484–4495.

Cruz Viggi, C., Rossetti, S., Fazi, S., Paiano, P., Majone, M., and Aulenta, F. (2014). Magnetite particles triggering a faster and more robust syntrophic pathway of methanogenic propionate degradation. Environ. Sci. Technol. *48*, 7536–7543.

Cui, H.-F., Du, L., Guo, P.-B., Zhu, B., and Luong, J.H.T. (2015). Controlled modification of carbon nanotubes and polyaniline on macroporous graphite felt for high-performance microbial fuel cell anode. J. Power Sources *283*, 46–53.

De Silva, K.K.H., Huang, H.H., Joshi, R.K., and Yoshimura, M. (2017). Chemical reduction of graphene oxide using green reductants. Carbon *119*, 190–199.

Du, Z., Li, H., and Gu, T. (2007). A state of the art review on microbial fuel cells: a promising technology for wastewater treatment and bioenergy. Biotechnol. Adv. *25*, 464–482.

Fan, M., Zhu, C., Feng, Z.Q., Yang, J., Liu, L., and Sun, D. (2014). Preparation of N-doped graphene by reduction of graphene oxide with mixed microbial system and its haemocompatibility. Nanoscale 6, 4882–4888.

Freyman, M.C., Kou, T., Wang, S., and Li, Y. (2020). 3D printing of living bacteria electrode. Nano Res. *13*, 1318–1323.

Geelhoed, J.S., and Stams, A.J. (2011). Electricity-assisted biological hydrogen production from acetate by *Geobacter sulfurreducens*. Environ. Sci. Technol. *45*, 815–820.

Gul, M.M., and Ahmad, K.S. (2019). Bioelectrochemical systems: sustainable bio-energy powerhouses. Biosens. Bioelectron. *142*, 111576.

Jiang, Y., Xu, Z., Huang, T., Liu, Y., Guo, F., Xi, J., Gao, W., and Gao, C. (2018). Direct 3D printing of ultralight graphene oxide aerogel microlattices. Adv. Funct. Mater. *28*, 1707024.

Jiang, H., Yang, L., Deng, W., Tan, Y., and Xie, Q. (2017). Macroporous graphitic carbon foam decorated with polydopamine as a high-

performance anode for microbial fuel cell. J. Power Sources 363, 27–33.

Katuri, K.P., Kavanagh, P., Rengaraj, S., and Leech, D. (2010). Geobacter sulfurreducens biofilms developed under different growth conditions on glassy carbon electrodes: insights using cyclic voltammetry. Chem. Commun. 46, 4758–4760.

Kumlanghan, A., Liu, J., Thavarungkul, P., Kanatharana, P., and Mattiasson, B. (2007). Microbial fuel cell-based biosensor for fast analysis of biodegradable organic matter. Biosens. Bioelectron. 22, 2939–2944.

Lee, B.-M., and Hur, J. (2016). Adsorption behavior of extracellular polymeric substances on graphene materials explored by fluorescence spectroscopy and two-dimensional fourier transform infrared correlation spectroscopy. Environ. Sci. Technol. 50, 7364–7372.

Lei, Z., Lu, L., and Zhao, X. (2012). The electrocapacitive properties of graphene oxide reduced by urea. Energ. Environ. Sci. 5, 6391–6399.

Li, D., Deng, L., Yuan, H., Dong, G., Chen, J., Zhang, X., Chen, Y., and Yuan, Y. (2018). N, P-doped mesoporous carbon from onion as trifunctional metal-free electrode modifier for enhanced power performance and capacitive manner of microbial fuel cells. Electrochim. Acta 262, 297–305.

Li, Y., Fu, Z.Y., and Su, B.L. (2012). Hierarchically structured porous materials for energy conversion and storage. Adv. Funct. Mater. 22, 4634–4667.

Liu, D., Chang, Q., Gao, Y., Huang, W., Sun, Z., Yan, M., and Guo, C. (2020). High performance of microbial fuel cell afforded by metallic tungsten carbide decorated carbon cloth anode. Electrochim. Acta 330, 135243.

Liu, P., Liang, P., Jiang, Y., Hao, W., Miao, B., Wang, D., and Huang, X. (2018). Stimulated electron transfer inside electroactive biofilm by magnetite for increased performance microbial fuel cell. Appl. Energ. 216, 382–388.

Logan, B.E., Rossi, R., and Saikaly, P.E. (2019). Electroactive microorganisms in bioelectrochemical systems. Nat. Rev. Microbiol. 17, 307–319.

Luo, S., Fu, B., Liu, F., He, K., Yang, H., Ma, J., Wang, H., Zhang, X., Liang, P., and Huang, X. (2020). Construction of innovative 3D-weaved carbon mesh anode network to boost electron transfer and microbial activity in bioelectrochemical system. Water Res. 172, 115493.

Lv, Z., Chen, Y., Wei, H., Li, F., Hu, Y., Wei, C., and Feng, C. (2013). One-step electrosynthesis of polypyrrole/graphene oxide composites for microbial fuel cell application. Electrochim. Acta 111, 366–373.

Mai, Y.J., Wang, X.L., Xiang, J.Y., Qiao, Y.Q., Zhang, D., Gu, C.D., and Tu, J.P. (2011). CuO/graphene composite as anode materials for lithium-ion batteries. Electrochim. Acta 56, 2306–2311.

Morris, J.M., and Jin, S. (2007). Feasibility of using microbial fuel cell technology for bioremediation of hydrocarbons in groundwater. J. Environ. Sci. Health A 43, 18–23.

Palanisamy, G., Jung, H.-Y., Sadhasivam, T., Kurkuri, M.D., Kim, S.C., and Roh, S.-H. (2019). A comprehensive review on microbial fuel cell technologies: processes, utilization, and advanced developments in electrodes and membranes. J. Clean. Prod. 221, 598–621.

Rahimnejad, M., Ghoreyshi, A.A., Najafpour, G., and Jafary, T. (2011). Power generation from organic substrate in batch and continuous flow microbial fuel cell operations. Appl. Energ. 88, 3999–4004.

Ren, H., Tian, H., Gardner, C.L., Ren, T.-L., and Chae, J. (2016). A miniaturized microbial fuel cell with three-dimensional graphene macroporous scaffold anode demonstrating a record power density of over $10000 \, W \, m^{-3}$. Nanoscale 8, 3539–3547.

Rusli, S.F.N., Bakar, M.H.A., Loh, K.S., and Mastar, M.S. (2019). Review of high-performance biocathode using stainless steel and carbon-based materials in microbial fuel cell for electricity and water treatment. Int. J. Hydrogen Energ. 44, 30772–30787.

Salas, E.C., Sun, Z., Luttge, A., and Tour, J.M. (2010). Reduction of graphene oxide via bacterial respiration. ACS Nano 4, 4852–4856.

Santoro, C., Arbizzani, C., Erable, B., and Ieropoulos, I. (2017). Microbial fuel cells: from fundamentals to applications. A review. J. Power Sources 356, 225–244.

Slate, A.J., Whitehead, K.A., Brownson, D.A.C., and Banks, C.E. (2019). Microbial fuel cells: an overview of current technology. Renew. Sust Energ. Rev. 101, 60–81.

Sun, H., Mei, L., Liang, J., Zhao, Z., Lee, C., Fei, H., Ding, M., Lau, J., Li, M., and Wang, C. (2017). Three-dimensional holey-graphene/niobia composite architectures for ultrahigh-rate energy storage. Science 356, 599–604.

Sun, M., Sheng, G.-P., Zhang, L., Xia, C.-R., Mu, Z.-X., Liu, X.-W., Wang, H.-L., Yu, H.-Q., Qi, R., and Yu, T. (2008). An MEC-MFC-coupled system for biohydrogen production from acetate. Environ. Sci. Technol. 42, 8095–8100.

Theodosiou, P., Greenman, J., and Ieropoulos, I. (2018). 3D-printable cathode electrode for monolithically printed microbial fuel cells (MFCs). In Proceedings of the 233rd Electrochemical Society (ECS) meeting), pp. 13–17.

Theodosiou, P., Greenman, J., and Ieropoulos, I.A. (2020). Developing 3D-printable cathode electrode for monolithically printed microbial fuel cells (MFCs). Molecules 25, 3635.

Virdis, B., and Dennis, P.G. (2017). The nanostructure of microbially-reduced graphene oxide fosters thick and highly-performing electrochemically-active biofilms. J. Power Sources 356, 556–565.

Wang, R., Yan, M., Li, H., Zhang, L., Peng, B., Sun, J., Liu, D., and Liu, S. (2018). FeS2 nanoparticles decorated graphene as microbial-fuel-cell anode achieving high power density. Adv. Mater. 30, 1800618.

Wang, Y., Zhao, C.-e., Sun, D., Zhang, J.-R., and Zhu, J.-J. (2013). A graphene/poly (3, 4-ethylenedioxythiophene) hybrid as an anode for high-performance microbial fuel cells. ChemPlusChem 78, 823.

Xu, H., Wang, L., Wen, Q., Chen, Y., Qi, L., Huang, J., and Tang, Z. (2019). A 3D porous NCNT sponge anode modified with chitosan and Polyaniline for high-performance microbial fuel cell. Bioelectrochemistry 129, 144–153.

Yuan, Y., Zhou, S., Liu, Y., and Tang, J. (2013). Nanostructured macroporous bioanode based on polyaniline-modified natural loofah sponge for high-performance microbial fuel cells. Environ. Sci. Technol. 47, 14525–14532.

Zhao, Y., Li, X., Ren, Y., and Wang, X. (2016). Effect of Fe (III) on the performance of sediment microbial fuel cells in treating waste-activated sludge. RSC Adv. 6, 47974–47980.

Zhao, D., Sun, K., Cheong, W.C., Zheng, L., Zhang, C., Liu, S., Cao, X., Wu, K., Pan, Y., and Zhuang, Z. (2019). Synergistically interactive pyridinic-N–MoP sites: identified active centers for enhanced hydrogen evolution in alkaline solution. Angew. Chem. Int. Edit 59, 8982–8990.

Zhao, X., Gao, W., Yao, W., Jiang, Y., Xu, Z., and Gao, C. (2017). Ion diffusion-directed assembly approach to ultrafast coating of graphene oxide thick multilayers. ACS Nano 11, 9663–9670.

Zhao, R., Jia, K., Wei, J.-J., Pu, J.-X., and Liu, X.-B. (2010). Hierarchically nanostructured Fe3O4 microspheres and their novel microwave electromagnetic properties. Mater. Lett. 64, 457–459.

Zhu, X., Yates, M.D., and Logan, B.E. (2012). Set potential regulation reveals additional oxidation peaks of Geobacter sulfurreducens anodic biofilms. Electrochem. Commun. 22, 116–119.

Supplemental information

Customizable design strategies

for high-performance bioanodes

in bioelectrochemical systems

Yu-Ting He, Qian Fu, Yuan Pang, Qing Li, Jun Li, Xun Zhu, Ren-Hao Lu, Wei Sun, Qiang Liao, and Uwe Schröder

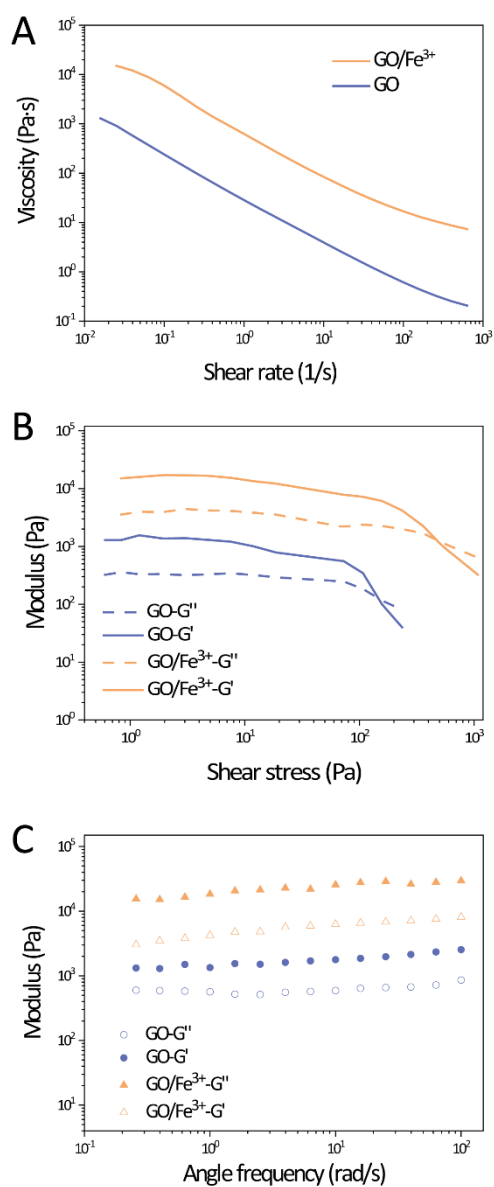**Supplemental Figures and Tables**

Figure S1. Rheological behaviors of printable GO inks. A) Rheological behaviors of the GO pure solution and GO gel ink. The storage modulus and loss modulus as functions of B) shear stress and C) angle frequency, Related to Figure 2.
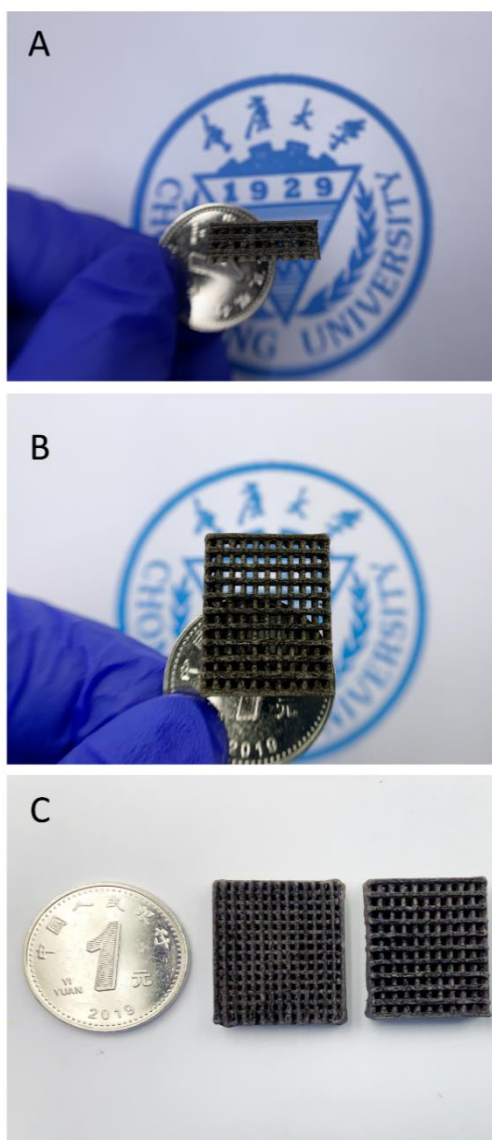
Figure S2. Morphology of 3D-printed $GO/Fe^{3+}/Fe_3O_4$ aerogel electrodes. Through-pore of 3D-printed $GO/Fe^{3+}/Fe_3O_4$ aerogel electrodes from A) top view and B) side view, respectively. C) Digital photos of different pore-size $GO/Fe^{3+}/Fe_3O_4$ aerogel electrodes, Related to Figure 2.
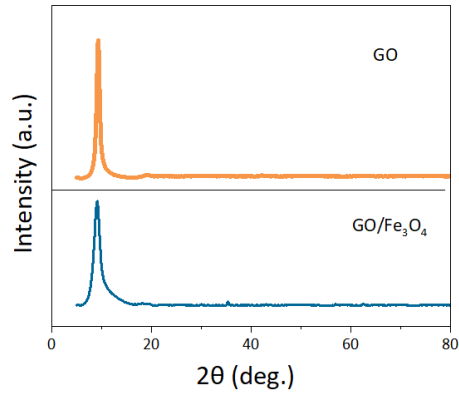
Figure S3. Full X-ray diffraction pattern spectrum of GO, GO/Fe^{3+}/Fe$_3$O$_4$ samples. The characteristic peaks at around 10.9° is indexed to the graphene oxide, Related to Figure 2.
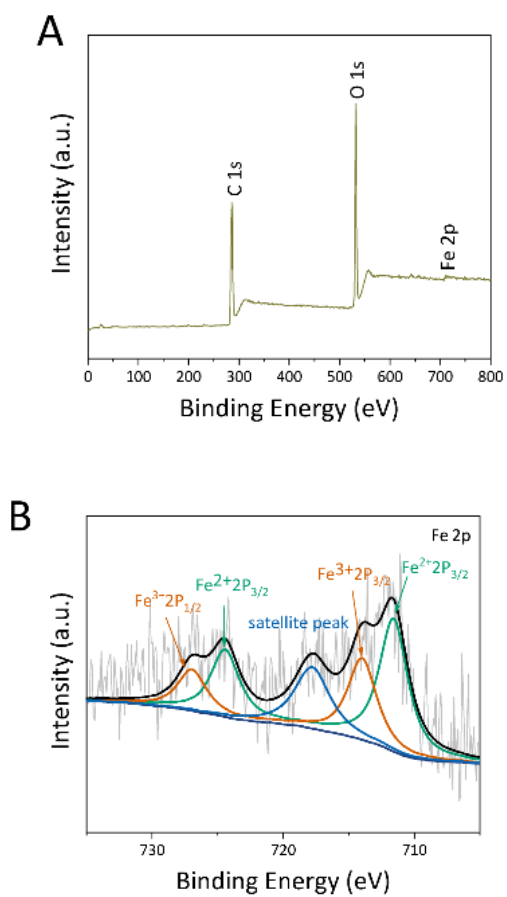
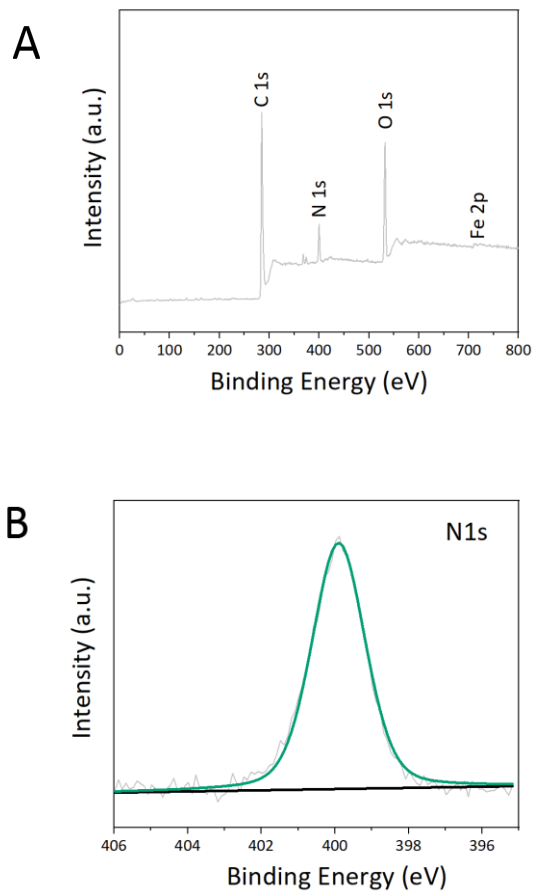**Figure S4**. XPS spectra of GO/Fe^{3+}/Fe_3O_4 electrode. A) Whole spectra and B) Fe 2p, Related to Figure 2.

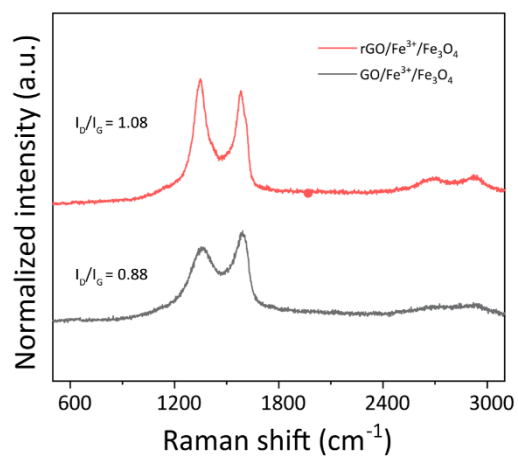**Figure S5.** XPS spectra of GO/Fe^{3+}/Fe_3O_4 electrode. A) Whole spectra and B) high resolution N1s, Related to Figure 2.

Figure S6. Raman spectroscopy of $GO/Fe^{3+}/Fe_3O_4$ and $rGO/Fe^{3+}/Fe_3O_4$ electrode. The obvious increase in the intensity ration of the D to G peak (I_D/I_G), indicating the restoration of sp^2 carbon in rGO sample, Related to Figure 3.
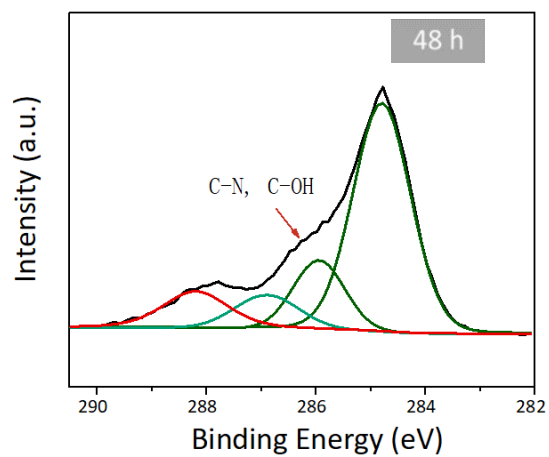
Figure S7. High resolution C1s XPS spectra of the interior of 3D-printed GO aerogel electrode after (48 h) the microbial reduction, Related to Figure 3.
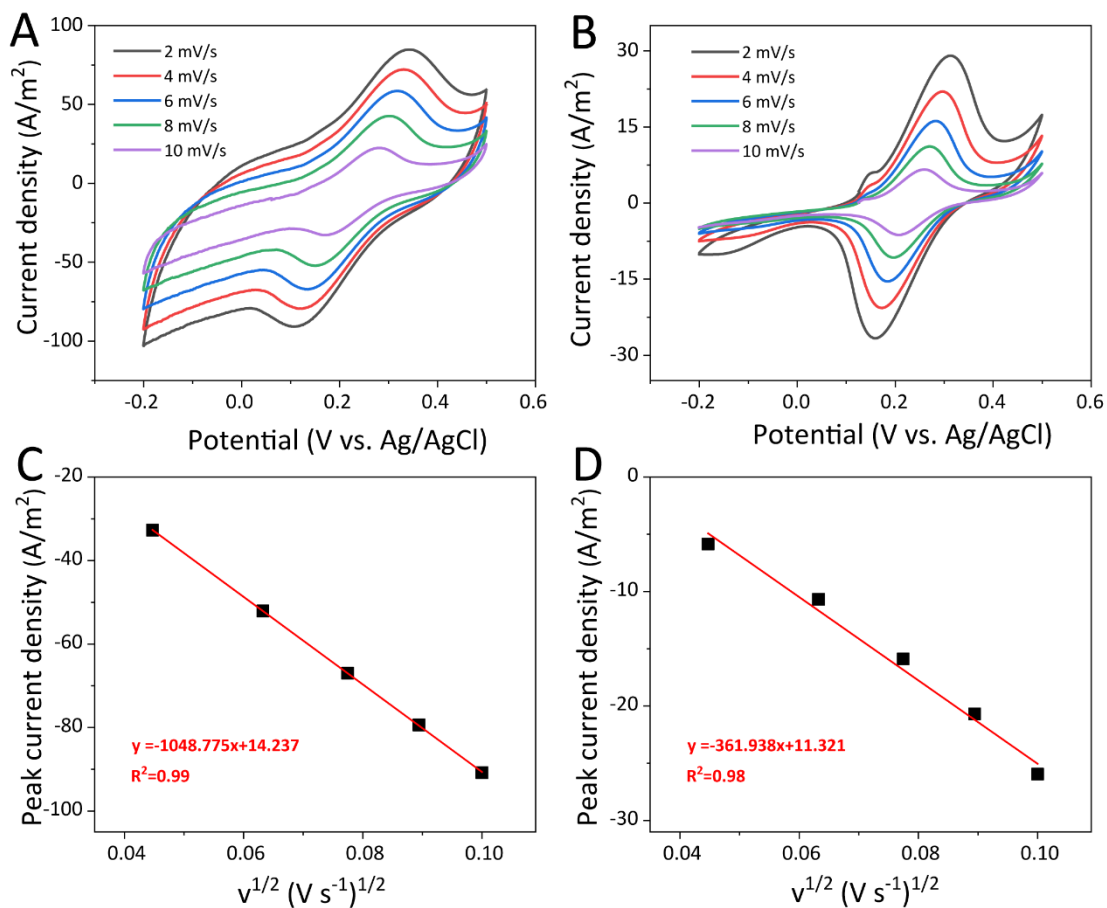
Figure S8. Electrochemically active surface areas of the 3D-printed rGO aerogel and carbon felt anode. A) CV diagrams of the 3D-printed rGO aerogel anode, and B) carbon felt anode collected at various small scan rates (2-10 mV s^{-1}) in 5 mM $K_3Fe(CN)_6$ containing 0.2 M Na_2SO_4 as supporting electrolyte. C) i_p vs. $v^{1/2}$ plots of the rGO aerogel anode, D) i_p vs. $v^{1/2}$ plots of carbon felt anode, Related to Figure 3.
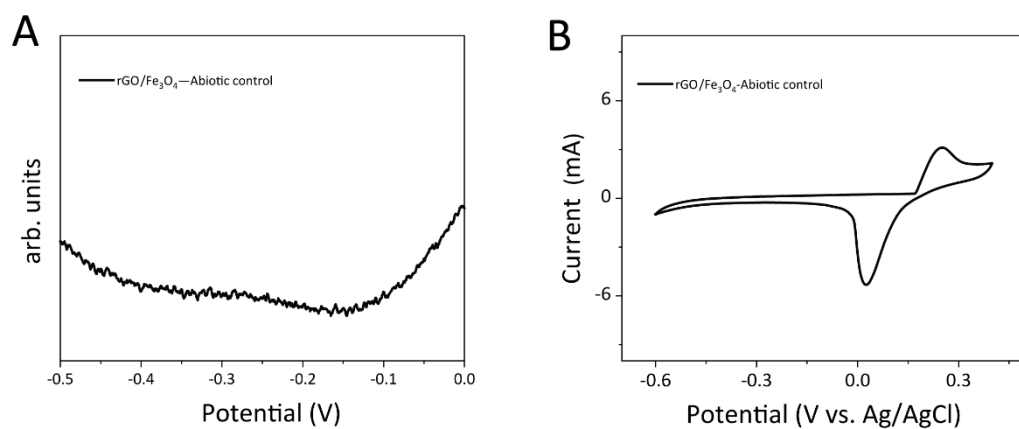
Figure S9. Electrochemical measurements of bare electrodes (without *G. sulfurreducens*). A) Differential pulse voltammetry, and B) cyclic voltammetry, Related to Figure 4.

Electrochemical Impedance Spectroscopy（EIS）analysis

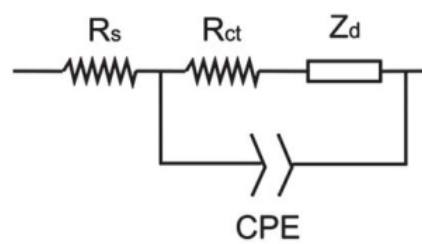**Figure S10**. The equivalent circuit of EIS, Related to Figure 4.
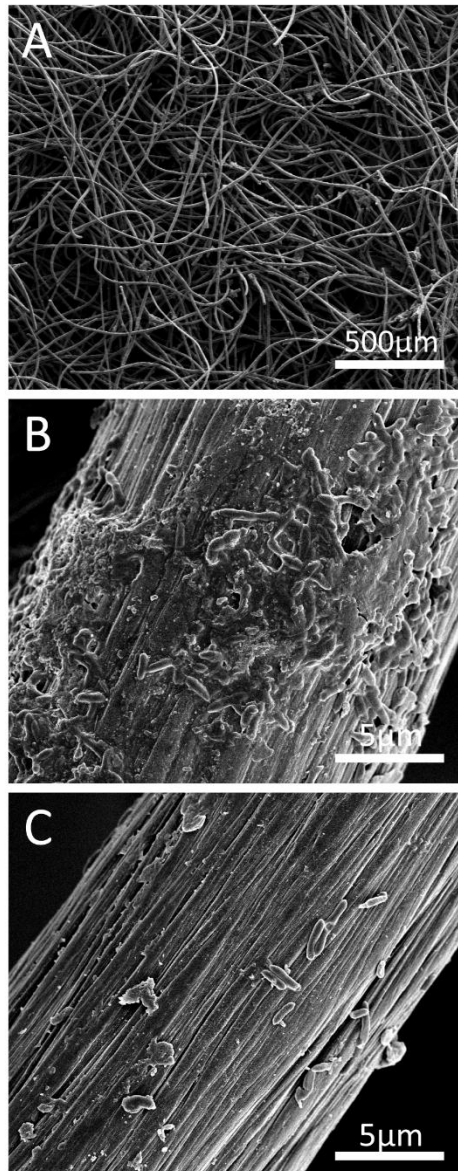
Figure S11. SEM images of biofilm formation of carbon felt anode. A-B) SEM images of outside, and C) inside carbon felt anode. The biofilm on the carbon felt surface produces relatively thick biofilm, while the biofilm inside of carbon felt is sparse, indicating the insufficient internal mass transfer of traditional 3D bioanodes, Related to Figure 6.

Figure S12. Replicated experiments of bioelectrochemical reactors using different anodes. A) Replication of rGO, rGO/Fe^{3+}, rGO/Fe_3O_4, $rGO/Fe^{3+}/Fe_3O_4$, and carbon felt electrodes. B) Replication of different channel size $rGO/Fe^{3+}/Fe_3O_4$ electrodes, Related to Figure 4 and Figure 5.

Table S1. ECSA of different electrodes in bioelectrochemical systems, Related to Figure 3.

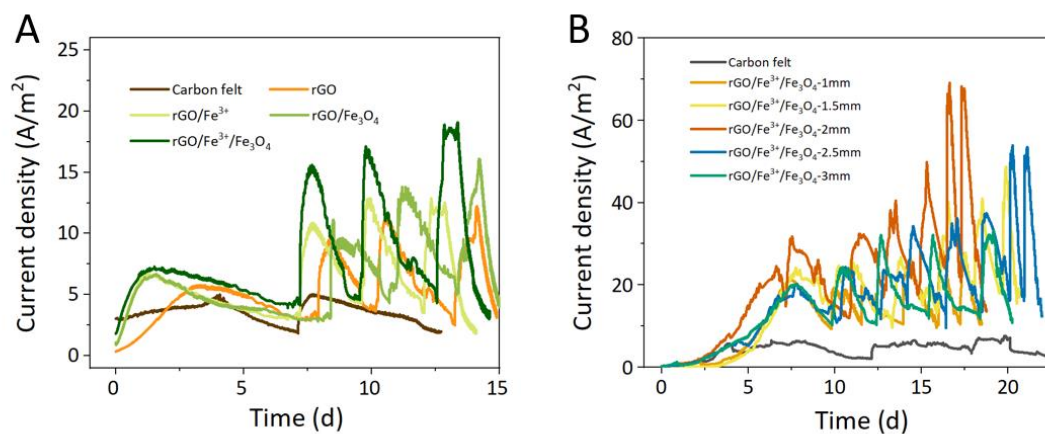| Electrode	Measurement conditions	Solution	[a] A (cm^2 cm^{-2})	Ref
Unmodified carbon cloth	Three-electrode system, 30 °C	5 mM $K_3[Fe(CN)_6]$, 0.2 M Na_2SO_4	1.68	(Li et al., 2020)
PDA/rGO-decorated carbon cloth	Three-electrode system, 30 °C	5 mM $K_3[Fe(CN)_6]$, 0.2 M Na_2SO_4	2.89	(Li et al., 2020)
PDDA/rGO-decorated carbon cloth	Three-electrode system, 30 °C	10 mM $K_3[Fe(CN)_6]$, 0.2 M Na_2SO_4	2.78	(Chen et al., 2020)
Stainless steel mesh	Three-electrode system, 35 °C	5 mM $K_3[Fe(CN)_6]$, 0.2 M Na_2SO_4	2.14	(Su et al., 2016)
3D stainless steel fiber felt	Three-electrode system, 35 °C	5 mM $K_3[Fe(CN)_6]$, 0.2 M Na_2SO_4	6.43	(Su et al., 2016)
Carbon felt	Three-electrode system, 30 °C	5 mM $K_3[Fe(CN)_6]$, 0.2 M Na_2SO_4	4.59	This work
3D-printed Fe_3O_4-decorated graphene	Three-electrode system, 30 °C	5 mM $K_3[Fe(CN)_6]$, 0.2 M Na_2SO_4	18.31	This work

PDA, polydopamine; PDDA, poly(diallyldimethylammonium chloride).

[a] ECSA normalized to the project surface area of anode.

Table S2. EIS fitting of the samples, Related to Figure 4.

Sample	Rs (Ω)	Rct (Ω)	Rw (Ω)
Carbon felt	6.192	15.45	2382
rGO	6.591	10.75	987
rGO/Fe^{3+}	5.696	10.67	896
rGO/Fe$_3$O$_4$	4.746	8.45	945
rGO/Fe^{3+}/Fe$_3$O$_4$	4.378	8.26	953

Table S3. EIS fitting of the samples, Related to Figure 5.

Sample	Rs (Ω)	Rct (Ω)	Rw (Ω)
Carbon felt	5.781	12.16	2854.2
rGO/Fe^{3+}/Fe_3O_4 -1mm	5.612	2.80	115.6
rGO/Fe^{3+}/Fe_3O_4 -1.5mm	3.023	1.29	11.0
rGO/Fe^{3+}/Fe_3O_4 -2mm	3.465	1.73	6.9
rGO/Fe^{3+}/Fe_3O_4 -2.5mm	3.647	2.65	6.5
rGO/Fe^{3+}/Fe_3O_4 -3mm	3.723	2.38	6.4

Transparent Methods

Chemicals and materials

Aqueous GO solution, which was synthesized using the modified Hummers method, was purchased from Suzhou Tanfeng Graphene Technology Co. Ltd (Suzhou, China) (Higginbotham et al., 2010). The concentration of the purchased GO aqueous dispersion was 10 mg/mL. The single GO sheets had a lateral dimension of $0.2 - 10$ µm and a vertical thickness of approximately 1 nm. All chemicals were of analytical reagent grade and were used without further purification. Deionized water was used in the experiments to obtain the anolyte and phosphate buffered saline (PBS).

Composite ink preparation of 3D-printed graphene anodes

First, the GO aqueous solution (10 mg/mL) was concentrated using centrifugation (3k-15, Sigma, Germany) at 9,500 rpm to obtain a higher concentration of 25 mg/mL. Two different kinds of GO-based inks were used to fabricate the anodes, with or without the addition of magnetite nanoparticles into the concentrated GO ink. The $FeCl_3$ aqueous solution was gradually added to the GO solution to form GO gel ink with constant stirring, and the final ferric ion concentration was about 12×10^{-3} M. The magnetite nanoparticles (2.4×10^{-3} M) were dispersed in the GO solution through ultrasonic oscillation to prepare a uniform suspension.

3D Printing of graphene anodes

The 3D electrodes were fabricated using GO gel through a low-temperature deposition manufacturing printer (LDM, BP11 from SunP Biotech, Biomanufacturing Center, Tsinghua University, China). The diameter of the printing nozzles was 210 µm. The 3D GO structures were printed onto a glass substrate at -15 °C to maintain their structure, with a scanning velocity of 12 mm s^{-1} and an injection velocity of 0.4 mm s^{-1}. Different channel sizes were set by different wire distances: 1, 1.5, 2, 2.5, and 3 mm. After printing, the 3D structure electrodes were transferred into a freezer (-80 °C) for further ice crystallization and sufficient assembly of GO sheets for 24 h. Finally, GO anodes were obtained after freeze-drying for 24 h using a freeze dryer (FD-1A-80, Christ, Germany).

Bioelectrochemical experiments and biofilm enrichment

Bioelectrochemical experiments were conducted under anaerobic conditions, and the 3D-printed graphene electrode served as a microbial fuel cell anode, with Ag/AgCl as the reference

electrode, and carbon felt was used as a counter electrode. The 3D-printed electrodes were mounted on a titanium mesh, which served as a current collector, and the 3D-printed electrodes and titanium mesh were connected by a conductive silver paste. The bacterium used for anode colonization was *G. sulfurreducens* (purchased from Leibniz-Institut DSMZ-Deutsche Sammlung von Mikroorganismen und Zellkulturen GmbH, Germany), which was grown in an acetate-feed medium containing 1,500 mg/L chemical oxygen demand (COD) and 50 mmol/L phosphate buffer solution. Two-chamber electrochemical cells were used in this study, each consisted of an anode and a cathode chamber with a volume of 250 mL. The Supporting experimental section includes detailed information on the anodic anaerobic medium and cathodic medium. The electrochemical cells were operated under fed-batch mode conditions at a constant temperature of 30 ± 1 °C. The working electrodes were poised at a constant potential of 50 mV *vs.* the Ag/AgCl reference electrode, with continuous stirring. All the potential lists in this study refer to the Ag/AgCl reference electrode, unless otherwise specified. Prior to operation, the bioelectrochemical reactor was inoculated with 50 mL of the precultured *G. sulfurreducens* suspension and 200 mL sterile anaerobic sodium acetate culture medium, which was purged with nitrogen for at least 30 min to ensure anoxic conditions. During the microbial reduction process, the reactor was kept under open-circuit conditions for 48 h at a constant temperature of 30 ± 1 °C with gentle mixing to allow the attachment and growth of *G. sulfurreducens,* as well as the concomitant formation of reduced graphene oxide (rGO). All experiments were performed at least twice.

Electrochemical measurement and analysis

Electrochemical characterization was performed using an electrochemical workstation (PMC-CHSO8A, AMETEK, Berwyn, USA) with a three-electrode system. Cyclic voltammetry (CV) was conducted to investigate the electrochemical properties of the 3D-printed electrodes under turnover conditions at a scanning rate of 0.1 mV/s with a range of -0.6 to 0.4 V. Prior to the measurements, the media was replaced with culture media containing 3.38 g/L acetate (Supporting Experimental Section, SI). Differential pulse voltammetry (DPV) was performed under non-turnover conditions (in the absence of acetate) by setting the following parameters: Pulse height of 50 mV, pulse width of 300 ms, step height of 0.5 mV, and step time of 2,000 ms (scan rate of 0.25 mV/s) (Marsili et al., 2010). The medium was replaced with 50 mM PBS, and the anode potential was set to 50 mV vs. Ag/AgCl to allow complete removal of the metabolic electrode donor. This induced cell starvation, which was monitored by a drop in the current density to values less than 0.1 mA. Electrochemical impedance spectroscopy (EIS)

measurements were also conducted in a three-electrode system after the bioelectrode reached a steady current generation, and the impedance spectra of the bioanodes recorded between 100 kHz and 10 mHz at an AC amplitude of 10 mV and working potential of 50 mV vs. Ag/AgCl.

X-ray diffraction (XRD) was performed to characterize the different-decorated rGO electrodes, from 5° to 80°, using an X-ray diffraction instrument (D8 ADVANCE, BRUCKER, Germany). X-ray photoelectron spectroscopy (XPS) was used to measure sample binding energy using a Thermo Scientific Escalab 250Xi. GO reduction was also measured using Raman spectroscopy (InVia Reflex, Renishaw, UK) under 532 nm laser excitation. Fourier transform infrared spectroscopy (FTIR, Nicolet iS10, Thermo Scientific, USA) was performed to analyze the chemical composition of GO, rGO electrode, and *G. sulfurreducens* samples in the frequency range of $500 - 4,000$ cm^{-1}. Prior to the FTIR test, the suspension of *G. sulfurreducens* was centrifuged (LYNX 4000, Thermo Fisher Scientific, USA) at 3,000 rpm for 5 min at room temperature, and the deposit then was freeze-dried at room temperature for 12 h to obtain the *G. sulfurreducens* samples. To obtain the rGO sample without bacteria, the rGO electrode was collected and washed ultrasonically with deionized water, 85% ethanol, 1 M HCl, and deionized water three times to remove the bacteria, followed by freeze-drying for 12 h at room temperature (Salas et al., 2010). A scanning electron microscope (SEM, S-4300N, Hitachi, Tokyo, Japan) was used to illustrate sample morphology (Supporting Experimental Section, SI). All measurements were performed at least twice.

The electroactive surface area (ECSA) was determined by CV measurements. A solution composed of 5 mM of $K_3[Fe(CN)_6]$ and 0.2 M of Na_2SO_4 was used as anolyte. The CVs were conducted over a range of -0.2–0.5 V at different scan rates of 2, 4, 6, 8, 10 mV s^{-1}. The ECSA of the working electrode (as-prepared anode) was obtained using Matsuda's equation (Liu et al., 2014):

$$i_p = 0.4464 \times 10^{-3} n^{3/2} F^{3/2} A (RT)^{-1/2} D^{1/2} C_0 v^{1/2}$$

where i_p represents the anodic peak current; n is the number of transferred electrons; F represents Faraday's constant (96,487 C mol^{-1}); R is the gas constant (8.314 J mol^{-1} K^{-1}); T is the temperature (303 K); A is the ECSA of the electrode; D represents the diffusion coefficient of the $K_3[Fe(CN)_6]$ solution (3.7×10^{-6} cm^2 s^{-1}) (Li et al., 2020); C_0 is the concentration of the $K_3[Fe(CN)_6]$ solution (5 mM); v is the scan rate.

Table S4 Measurement uncertainties, Related to Figure 3, 4 and 5.

	Source	Range	Error
Constant potential	PMC-CHSO8A, AMETEK	± 10 V	± 0.2% of value
Voltage measurement	PMC-CHSO8A, AMETEK	± 10 V	± 0.2% of reading
Current measurement	PMC-CHSO8A, AMETEK	1 A	± 0.2% of reading

Microbial culture medium preparation.

Culture medium was sterilized in an autoclave at 121°C for 30 min and then placed in the incubator at 32 °C for 24 h before using.

Per liter, the anodic anaerobic medium contains:

$Na_2HPO_4 \cdot H_2O$	11.8 g
KH_2PO_4	2.7 g
$CH_3COONa \cdot 3H_2O$	3.38 g
NaCl	0.5 g
NH_4Cl	0.1 g
$MgSO_4 \cdot 7H_2O$	0.1 g
$CaCl_2 \cdot 2H_2O$	15 mg
Trace element solution	1 mL

Per liter, the trace element solution contains:

$FeSO_4 \cdot 7H_2O$	1 g
$ZnCl_2$	70 mg
$MnCl_2 \cdot 4H_2O$	100 mg
H_3BO_3	6 mg
$CaCl_2 \cdot 6H_2O$	130 mg
$CuCl_2 \cdot 2H_2O$	2 mg
$NiCl_2 \cdot 6H_2O$	24 mg
$Na_2MoO_2 \cdot 2H_2O$	36 mg
$CoCl_2 \cdot 6H_2O$	238mg

Cathodic medium preparation

Cathodic medium was 50 mM phosphate buffer solution containing 11.8 g L^{-1} $Na_2HPO_4 \cdot H_2O$, 2.7 g L^{-1} KH_2PO_4, pH = 7.2 and 50 mM ferricyanide.

SEM sample preparation process

Before the SEM analysis, the samples of bioanodes were firstly fixed with 2.5% glutaraldehyde solution for 2 h at 4 °C in a refrigerator. Then the samples were washed with graded-ethanol series (30%, 50%, 70%, 80%, 90%, and 100%) for 15 min at each concentration, and graded-tert butyl alcohol series (70%, 80%, 90%, and 95%) for 10 minutes at each concentration. Finally, the samples were dried thoroughly in a constant temperature of 30 °C.

Supplemental References

Chen, X., Li, Y., Yuan, X., Li, N., He, W., and Liu, J. (2020). Synergistic effect between poly (diallyldimethylammonium chloride) and reduced graphene oxide for high electrochemically active biofilm in microbial fuel cell. Electrochim Acta. 359, 136949.

Higginbotham, A.L., Kosynkin, D.V., Sinitskii, A., Sun, Z., and Tour, J.M. (2010). Lower-defect graphene oxide nanoribbons from multiwalled carbon nanotubes. ACS Nano. 4(4), 2059-2069.

Li, Y., Liu, J., Chen, X., Yuan, X., Li, N., He, W., and Feng, Y. (2020). Enhanced electricity generation and extracellular electron transfer by polydopamine–reduced graphene oxide (PDA–rGO) modification for high-performance anode in microbial fuel cell. Chem Eng J. 387, 123408.

Liu, J., Liu, J., He, W., Qu, Y., Ren, N., and Feng, Y. (2014). Enhanced electricity generation for microbial fuel cell by using electrochemical oxidation to modify carbon cloth anode. J Power Sources. 265, 391-396.

Marsili, E., Sun, J., and Bond, D.R. (2010). Voltammetry and growth physiology of *Geobacter sulfurreducens* biofilms as a function of growth stage and imposed electrode potential. Electroanalysis. 22(7‐8), 865-874.

Salas, E.C., Sun, Z., Luttge, A., and Tour, J.M. (2010). Reduction of graphene oxide via bacterial respiration. ACS nano. 4(8), 4852-4856.

Su, M., Wei, L., Qiu, Z., Wang, G., and Shen, J. (2016). Hydrogen production in single chamber microbial electrolysis cells with stainless steel fiber felt cathodes. J Power Sources. 301, 29-34.